# A plasticity model and algorithm for mode-I cracking in concrete

INTERNATIONAL JOURNAL FOR NUMERICAL METHODS IN ENGINEERING, VOL. 38, 2509–2529 (1995)

# A PLASTICITY MODEL AND ALGORITHM FOR MODE-I CRACKING IN CONCRETE

PETER H. FEENSTRA AND RENÉ DE BORST*

*Delft University of Technology, Faculty of Civil Engineering, P.O. Box 5048, 2600 GA Delft, The Netherlands*

## SUMMARY

A class of plasticity models which utilize Rankine's (principal stress) yield locus is formulated to simulate cracking in concrete and rock under monotonic loading conditions. The formulation encompasses isotropic and kinematic hardening/softening rules, and incremental (flow theory) as well as total (deformation theory) formats are considered. An Euler backward algorithm is used to integrate the stresses and internal variables over a finite loading step and an explicit expression is derived for a consistently linearized tangent stiffness matrix associated with the Euler backward scheme. Particular attention is paid to the corner regime, that is when the two major principal stresses become equal. A detailed comparison has been made of the proposed plasticity-based crack formulations and the traditional fixed and rotating smeared-crack models for a homogeneously stressed sample under a non-proportional loading path. A comparison between the flow-theory-based plasticity crack models and experimental data has been made for a Single Edge Notched plain concrete specimen under mixed-mode loading conditions.

KEY WORDS: concrete; cracking; fracture; mode-I; plasticity; softening

## INTRODUCTION

Since the first applications of non-linear finite element analyses to concrete structures in the late 1960s,[1,2] many new developments and improvements have been published. This holds true for the discrete crack approaches, where the interior of the structure is kept linear elastic and crack propagation is simulated by changing the topology of the structure, as well as for the smeared-crack approach, on which class of crack models our attention will be focused in this contribution. In smeared-crack models, it is assumed that the non-linearities due to cracking can be distributed over an area that belongs to a sampling point in a numerically integrated finite element. Cracking is then monitored via certain internal parameters which are updated in the sampling point upon progressive cracking.

In the first use of the smeared-crack approach by Rashid,[1] the major principal stress was set equal to zero immediately upon violation of the tensile strength of the concrete. Also, the shear capacity in this direction was assumed to have vanished, and a zero shear stiffness was inserted in the anisotropic elastic stress–strain relation. Later, enhancements were proposed like the partial retention of shear stiffness across the crack face via a shear retention factor,[3] and the gradual decrease of the tensile carrying capacity in the direction normal to the crack instead of the sudden drop to zero adopted originally. In this contribution, we shall focus on a side effect of the

* Also at Eindhoven University of Technology, Faculty of Mechanical Engineering

CCC 0029–5981/95/152509–21

*Received 25 February 1994*
*Revised 12 September 1994*

introduction of a shear retention factor and a softening branch, namely the fact that the principal stress direction after cracking now no longer coincides with the normal to the crack and that the major principal stress may even exceed the tensile strength in another direction. Neglecting this effect causes spurious stresses to occur and tends to result in collapse loads that severely overestimate the true failure load.

Probably, this phenomenon was first recognized by Cope *et al.*,[4] who, in an engineering approach, suggested to corotate the crack axes with the axes of the principal stress directions. A direct consequence of this approach is that the shear stiffness can no longer be specified independently, but, under the physically realistic assumption of coaxiality of stress and strain tensors, becomes an implicit function of the rotation of the principal stress axes. In a different approach, de Borst, Nauta and Rots[5–8] departed from the total stress–strain relations employed hitherto, and changed to an incremental formulation. In this approach, they assigned a part of the strain increment to the uncracked concrete, and a part to each individual crack (primary, secondary, etc.). The advantages of the model over the rotating crack approach are that it allows for a transparent combination with other non-linear phenomena, such as creep, shrinkage and thermal loading,[7] and that it incorporates path-dependent behaviour which in principle can properly accommodate non-proportional loadings. Disadvantages of the model are the complications involved in programming the model properly, the fact that a robust algorithm could not be devised for cases where both cracking and plasticity (which arises due to large compressive stresses parallel to the cracks) occur in one sampling point, and the numerical difficulties that appeared during state changes.[9]

To solve both the problem of the overestimation of the failure load and the numerical difficulties associated with the multiple-crack model,[5–8] a constitutive model has been developed which describes the formation of cracks within the framework of plasticity theory. Rankine's (principal stress) yield criterion is invoked to initiate cracking and to monitor crack propagation. Since tensile loading in one direction leaves the tensile capacity intact in the transverse direction, the evolution of the yield locus by an isotropic hardening/softening rule is questionable and therefore the use of a kinematic hardening/softening rule has been investigated as well. Furthermore, in addition to the flow theory of plasticity that has been employed, the Rankine plasticity model with kinematic/isotropic hardening/softening has been developed into an algorithmic setting also for a deformation theory of plasticity. The latter model will be discussed to show the analogy with the rotating crack model.

This paper is ordered as follows. Firstly, a concise description is given of the integration of a flow theory of plasticity using an Euler backward scheme. Then, the algorithmic treatment is specialized to the Rankine yield criterion. For use within the framework of the Newton–Raphson method the stress–strain relation for finite increments is consistently linearized. It is shown how, with some minor modifications, the algorithm can be used to simulate a deformation theory of plasticity. Next, a comparison is made of the proposed plasticity-based crack formulations and the traditional fixed and rotating smeared-crack models for a homogeneously stressed sample under a non-proportional loading path. Finally, finite element simulations using the Rankine flow theory are compared with experimental data for a Single Edge Notched (SEN) plain concrete specimen under mixed-mode loading conditions.

## INCREMENTAL FORMULATION

Assuming small strains, we adopt the additive decomposition of the strain rate vector $\dot{\boldsymbol{\varepsilon}}$ into an elastic, reversible part $\dot{\boldsymbol{\varepsilon}}_e$ and an inelastic, irreversible part $\dot{\boldsymbol{\varepsilon}}_c$,

$$\dot{\boldsymbol{\varepsilon}} = \dot{\boldsymbol{\varepsilon}}_e + \dot{\boldsymbol{\varepsilon}}_c \tag{1}$$

The elastic strain rate determines the stress rate through the elastic stiffness ratio matrix $\mathbf{D}_e$, which is assumed to be isotropic throughout this article,

$$\dot{\boldsymbol{\sigma}} = \mathbf{D}_e \dot{\boldsymbol{\varepsilon}}_e \tag{2}$$

The evolution of the inelastic strain is dependent upon the assumption of the constitutive model and is in general a function of the stress and strain state and the internal variables. The inelastic strain rate will now be determined with an incremental formulation based on the flow theory of plasticity.

A fundamental notion of plasticity theory is the existence of a yield function

$$f(\boldsymbol{\sigma}, \boldsymbol{\eta}, \mathbf{q}) = 0 \tag{3}$$

which depends on the stress vector $\boldsymbol{\sigma}$, the back-stress vector $\boldsymbol{\eta}$, which allows for a kinematic hardening behaviour, and on a number of scaled-valued internal variables, conveniently collected in a vector $\mathbf{q}$. The evolution of the inelastic strain rate is given by the associated flow rule

$$\dot{\boldsymbol{\varepsilon}}_c = \dot{\lambda} \partial_\sigma f \tag{4}$$

where the notation $\partial_\sigma f$ is used to denote the derivative of the yield function $f$ with respect to the stress vector $\boldsymbol{\sigma}$. The rate of the inelastic multiplier $\dot{\lambda}$ has to comply with the Kuhn–Tucker conditions

$$\dot{\lambda} \geqslant 0, \quad f \leqslant 0, \quad \dot{\lambda} f = 0 \tag{5}$$

The evolution of the back stress is assumed to be given by a generalization of Prager's kinematic hardening rule with the direction of the back-stress rate determined by a function $g$,

$$\dot{\boldsymbol{\eta}} = (1 - \gamma) E_k \dot{\lambda} \partial_\sigma g \tag{6}$$

in which $E_k$ is the kinematic tangential hardening modulus and $\gamma$ is the proportion of isotropic and kinematic hardening, $\gamma = 0$ implying full kinematic hardening and $\gamma = 1$ setting the other limiting case of pure isotropic hardening. The evolution of the internal variable vector is assumed to be given by a general evolutionary equation

$$\dot{\mathbf{q}} = \dot{\lambda} \mathbf{h}(\boldsymbol{\sigma}, \boldsymbol{\eta}, \mathbf{q}) \tag{7}$$

The evolution equations given above can be regarded as strain-driven in the sense that the total strain vector, the inelastic strain vector and the internal variables are known at time $t$, and that the incremental strain vector $\Delta\boldsymbol{\varepsilon}^{(i+1)}$ in the current iteration $i+1$ follows from the loading regime. The basic problem in computational elastoplasticity is that the elastoplastic constitutive equations have to be updated in a consistent manner:

$$({}^t\boldsymbol{\sigma}, {}^t\boldsymbol{\varepsilon}, {}^t\boldsymbol{\eta}, {}^t\mathbf{q}; \Delta\boldsymbol{\varepsilon}^{(i+1)}) \rightarrow (\boldsymbol{\sigma}^{(i+1)}, \boldsymbol{\varepsilon}^{(i+1)}, \boldsymbol{\eta}^{(i+1)}, \mathbf{q}^{(i+1)})$$

By applying the fully implicit Euler backward algorithm, this problem is transformed into a constrained optimization problem governed by discrete Kuhn–Tucker conditions.[10] It has been shown in different studies[11–14] that the implicit Euler backward algorithm is stable and accurate for $J_2$-plasticity. But even when the yield surface is highly distorted, the Euler backward algorithm is unconditionally stable and accurate.[14–16] Application of the Euler backward

algorithm results in a discrete set of equations:

$$\begin{aligned}
\boldsymbol{\varepsilon}^{(i+1)} &= {}^{t}\boldsymbol{\varepsilon} + \Delta\boldsymbol{\varepsilon}^{(i+1)} \\
\boldsymbol{\sigma}^{(i+1)} &= \mathbf{D}_e(\boldsymbol{\varepsilon}^{(i+1)} - \boldsymbol{\varepsilon}_c^{(i+1)}) \\
\boldsymbol{\varepsilon}_c^{(i+1)} &= {}^{t}\boldsymbol{\varepsilon}_c + \Delta\lambda^{(i+1)}\partial_\sigma f^{(i+1)} \\
\mathbf{q}^{(i+1)} &= {}^{t}\mathbf{q} + \Delta\lambda^{(i+1)}\mathbf{h}^{(i+1)} \\
\boldsymbol{\eta}^{(i+1)} &= {}^{t}\boldsymbol{\eta} + \Delta\lambda^{(i+1)}(1-\gamma)E_{ks}\partial_\sigma g^{(i+1)}
\end{aligned} \tag{8}$$

with $E_{ks}$ the secant hardening modulus. The discrete Kuhn–Tucker conditions read

$$\begin{aligned}
\Delta\lambda^{(i+1)} &\geqslant 0 \\
f(\boldsymbol{\sigma}^{(i+1)}, \boldsymbol{\eta}^{(i+1)}, \mathbf{q}^{(i+1)}) &\leqslant 0 \\
\Delta\lambda^{(i+1)} f(\boldsymbol{\sigma}^{(i+1)}, \boldsymbol{\eta}^{(i+1)}, \mathbf{q}^{(i+1)}) &= 0
\end{aligned} \tag{9}$$

Because the algorithm is considered within an elastic-predictor–plastic-corrector algorithm, an elastic trial state is introduced as

$$\begin{aligned}
\boldsymbol{\varepsilon}_E &= {}^{t}\boldsymbol{\varepsilon}_e + \Delta\boldsymbol{\varepsilon}^{(i+1)} \\
\boldsymbol{\sigma}_E &= \mathbf{D}_e\boldsymbol{\varepsilon}_E \\
\boldsymbol{\eta}_E &= {}^{t}\boldsymbol{\eta} \\
\mathbf{q}_E &= {}^{t}\mathbf{q}
\end{aligned} \tag{10}$$

which can be obtained by freezing inelastic flow during the time step.

## A RANKINE FLOW THEORY

The maximum tensile stress criterion of Rankine will be used to bound the tensile strength of concrete. Consider a plane-stress situation in which the major principal stress $\sigma_1$ is defined by means of Mohr's circle, Figure 1. The hardening behaviour is assumed to be described by an internal variable $\kappa$ which governs the major principal stress. The yield function is then

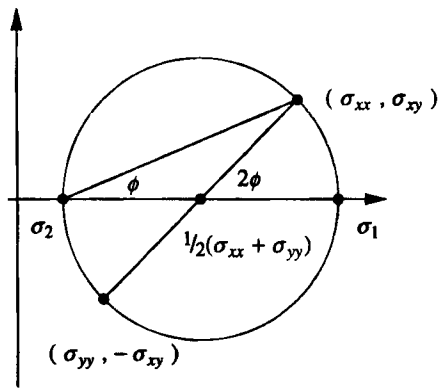


Figure 1. Mohr's circle

given by

$$f = \sigma_1 - \bar{\sigma}(\kappa) \tag{11}$$

In the formulation presented here, a single stress-based function is defined which is governed by the major principal stress, and with an equivalent stress which describes the hardening behaviour of the material. The assumption of isotropic behaviour is not completely valid for a material which is intrinsically anisotropic since it can be loaded to the virgin tensile strength even if in the transverse direction the stress has been reduced due to softening of the material. For this reason, a kinematic hardening model in which the yield surface is shifted in the direction of the major principal stress may be more adequate for modelling fracture in concrete.

In a plane-stress configuration with an expanded stress vector $\boldsymbol{\sigma}^{\mathrm{T}} = \{\sigma_{xx}, \sigma_{yy}, \sigma_{zz}, \sigma_{xy}\}$, the major principal stress can be expressed in terms of the stress vector with the aid of Mohr's circle. This results in a yield function with mixed hardening, which reads

$$f = (\tfrac{1}{2}\boldsymbol{\xi}^{\mathrm{T}}\mathbf{P}\boldsymbol{\xi})^{1/2} + \tfrac{1}{2}\boldsymbol{\pi}^{\mathrm{T}}\boldsymbol{\xi} - \bar{\sigma}(\gamma\kappa) \tag{12}$$

with the reduced stress $\boldsymbol{\xi} = \boldsymbol{\sigma} - \boldsymbol{\eta}$ and the equivalent stress $\bar{\sigma}$ as a function of the internal parameter $\kappa$. With $\boldsymbol{\xi}^{\mathrm{T}} = \{\xi_{xx}, \xi_{yy}, \xi_{zz}, \xi_{xy}\}$, the projection matrix $\mathbf{P}$ and the projection vector $\boldsymbol{\pi}$ are given by

$$\mathbf{P} = \begin{bmatrix} \frac{1}{2} & -\frac{1}{2} & 0 & 0 \\ -\frac{1}{2} & \frac{1}{2} & 0 & 0 \\ 0 & 0 & 0 & 0 \\ 0 & 0 & 0 & 2 \end{bmatrix} \tag{13}$$

and

$$\boldsymbol{\pi} = \{1, 1, 0, 0\}^{\mathrm{T}} \tag{14}$$

respectively. The equivalent stress $\bar{\sigma}(\gamma\kappa)$ is the uniaxial tensile strength which is assumed to be given by a non-linear function of the internal parameter $\kappa$.

The incremental back-stress vector has been defined in equation (8) as

$$\Delta\boldsymbol{\eta} = \Delta\lambda(1 - \gamma)E_{\mathrm{ks}}\partial_{\sigma}g$$

in which the direction of the incremental back-stress vector is determined by the derivative of a function $g$ with respect to the stress vector at the final stress. Assuming that the direction of the incremental back-stress vector is given by the major principal stress direction at the final stress, $g$ can be determined. Consider the following expression in which the stress vector $\boldsymbol{\sigma}$ is expressed as a transformation of the principal stress vector:

$$\boldsymbol{\sigma} = \sigma_1 \begin{Bmatrix} \cos^2\phi \\ \sin^2\phi \\ 0 \\ \sin\phi\cos\phi \end{Bmatrix} + \sigma_2 \begin{Bmatrix} \sin^2\phi \\ \cos^2\phi \\ 0 \\ -\sin\phi\cos\phi \end{Bmatrix} + \sigma_3 \begin{Bmatrix} 0 \\ 0 \\ 1 \\ 0 \end{Bmatrix} \tag{15}$$

The direction of the incremental back-stress vector is now assumed to be given by the direction vector which is related to the major principal stress $\sigma_1$, so

$$\Delta\boldsymbol{\eta} = \Delta\lambda(1-\gamma)E_{ks}\begin{Bmatrix}\cos^2\phi\\ \sin^2\phi\\ 0\\ \sin\phi\cos\phi\end{Bmatrix} \tag{16}$$

We now note that the gradient to the yield function

$$\partial_\sigma f = \frac{\mathbf{P}\boldsymbol{\xi}}{2(\frac{1}{2}\boldsymbol{\xi}^T\mathbf{P}\boldsymbol{\xi})^{1/2}} + \frac{1}{2}\boldsymbol{\pi} \tag{17}$$

can be expressed in terms of the angle between the normal directions and the principal directions:

$$\partial_\sigma f = \begin{Bmatrix}\frac{1}{2}+\frac{1}{2}\cos 2\phi\\ \frac{1}{2}-\frac{1}{2}\cos 2\phi\\ 0\\ \sin 2\phi\end{Bmatrix} = \begin{Bmatrix}\cos^2\phi\\ \sin^2\phi\\ 0\\ 2\sin\phi\cos\phi\end{Bmatrix} \tag{18}$$

see also Figure 1 for the definition of the angle $\phi$. Comparing equations (16) and (18) we observe that

$$\Delta\boldsymbol{\eta} = \Delta\lambda(1-\gamma)E_{ks}\boldsymbol{\Lambda}_M\partial_\sigma f \tag{19}$$

where

$$\boldsymbol{\Lambda}_M = \mathrm{diag}[1,1,1,\tfrac{1}{2}] \tag{20}$$

It is assumed that the internal damage in the material as reflected in the internal parameter $\kappa$ is governed by a work-hardening hypothesis. In a work-hardening hypothesis the internal variable is determined by the inelastic work rate $\dot{W}_c$ defined by

$$\dot{W}_c = \boldsymbol{\xi}^T\dot{\boldsymbol{\varepsilon}}_c = \bar{\sigma}(\gamma\kappa)\dot{\kappa} \tag{21}$$

or, utilizing Euler's theorem, we obtain

$$\dot{\kappa} = \dot{\lambda} \tag{22}$$

so that for finite loading steps the general evolutionary equation, equation (7), simplifies to

$$\Delta\kappa = \Delta\lambda \tag{23}$$

in the case of the Rankine yield criterion.

The updated stress vector $\boldsymbol{\sigma}^{(i+1)}$ and the updated back-stress vector $\boldsymbol{\eta}^{(i+1)}$ are obtained by substituting equations (10), (17) and (19) into the discrete set of equations, equation (8). This results in

$$\begin{Bmatrix}\boldsymbol{\sigma}^{(i+1)}\\ \boldsymbol{\eta}^{(i+1)}\end{Bmatrix} = \begin{bmatrix}\mathbf{A}_{11} & \mathbf{A}_{12}\\ \mathbf{A}_{21} & \mathbf{A}_{22}\end{bmatrix}^{-1}\begin{Bmatrix}\boldsymbol{\sigma}_E - \frac{1}{2}\Delta\lambda^{(i+1)}\mathbf{D}_e\boldsymbol{\pi}\\ \boldsymbol{\eta}_E + \frac{1}{2}\Delta\lambda^{(i+1)}(1-\gamma)E_{ks}\boldsymbol{\pi}\end{Bmatrix} \tag{24}$$

with the matrices

$$\mathbf{A}_{11} = \mathbf{I} + \frac{\Delta\lambda^{(i+1)}}{2\Psi}\mathbf{D}_e\mathbf{P}$$

$$\mathbf{A}_{12} = -\frac{\Delta\lambda^{(i+1)}}{2\Psi}\mathbf{D}_e\mathbf{P}$$

$$\mathbf{A}_{21} = -\frac{\Delta\lambda^{(i+1)}}{2\Psi}(1-\gamma)E_{ks}\boldsymbol{\Lambda}_M\mathbf{P}$$

$$\mathbf{A}_{22} = \mathbf{I} + \frac{\Delta\lambda^{(i+1)}}{2\Psi}(1-\gamma)E_{ks}\boldsymbol{\Lambda}_M\mathbf{P}$$

where the denominator $\Psi$ is defined as

$$\Psi = (\tfrac{1}{2}\boldsymbol{\xi}^{(i+1)^T}\mathbf{P}\boldsymbol{\xi}^{(i+1)})^{1/2} \tag{25}$$

Equation (25) for $\Psi$ is not very convenient because the updated stress in equation (24) is then not related linearly to the trial state. To arrive at a more suitable form we express the denominator $\Psi$ in terms of the inelastic multiplier via premultiplication of $\boldsymbol{\sigma}^{(i+1)}$ and $\boldsymbol{\eta}^{(i+1)}$ by $\boldsymbol{\pi}^T$ (Reference 18):

$$\begin{aligned}\boldsymbol{\pi}^T\boldsymbol{\sigma}^{(i+1)} &= \boldsymbol{\pi}^T\boldsymbol{\sigma}_E - \tfrac{1}{2}\Delta\lambda^{(i+1)}\boldsymbol{\pi}^T\mathbf{D}_e\boldsymbol{\pi}\\ \boldsymbol{\pi}^T\boldsymbol{\eta}^{(i+1)} &= \boldsymbol{\pi}^T\boldsymbol{\eta}_E + \tfrac{1}{2}\Delta\lambda^{(i+1)}(1-\gamma)\boldsymbol{\pi}^T E_{ks}\boldsymbol{\pi}\end{aligned} \tag{26}$$

because $\boldsymbol{\pi}^T\mathbf{D}_e\mathbf{P} = \mathbf{0}^T$. The denominator now reads

$$\Psi = \bar{\sigma}(\gamma\kappa) - \frac{1}{2}\boldsymbol{\pi}^T(\boldsymbol{\sigma}_E - \boldsymbol{\eta}_E) + \frac{1}{2}\Delta\lambda^{(i+1)}\left(\frac{E}{(1+\nu)(1-2\nu)} + (1-\gamma)E_{ks}\right) \tag{27}$$

and is expressed solely in terms of the variables in the trial state and the inelastic multiplier. Accordingly, equation (24) is a linear system of equations in the unknowns $\boldsymbol{\sigma}^{(i+1)}$ and $\boldsymbol{\eta}^{(i+1)}$.

The matrix defined in equation (24) will henceforth be denoted as the mapping matrix. The calculation of the mapping matrix can result in numerical problems because the calculation of the submatrices of the mapping matrix involves a division by $\Psi$. This factor becomes equal to zero in the corner of the yield surface. However, if $\Psi$ is equal to zero, the inverted mapping matrix is still defined, which can be shown by application of a spectral decomposition of the submatrices.[3,19] The algorithm for the regular region of the yield surface will be derived below and the corner regime will be discussed in the Appendix.

Because of the assumption of isotropic elasticity, it appears that the linear-elastic stiffness matrix $\mathbf{D}_e$ and the projection matrix $\mathbf{P}$ have the same eigenvector space. This means that the spectral decomposition is given by the same transformation matrix, according to

$$\mathbf{D}_e = \mathbf{Q}\boldsymbol{\Lambda}_D\mathbf{Q}^T \tag{28}$$

and

$$\mathbf{P} = \mathbf{Q}\boldsymbol{\Lambda}_P\mathbf{Q}^T \tag{29}$$

with the orthogonal matrix

$$\mathbf{Q} = \begin{bmatrix} \frac{1}{\sqrt{6}} & \frac{-1}{\sqrt{2}} & \frac{1}{\sqrt{3}} & 0 \\ \frac{1}{\sqrt{6}} & \frac{1}{\sqrt{2}} & \frac{1}{\sqrt{3}} & 0 \\ \frac{-2}{\sqrt{6}} & 0 & \frac{1}{\sqrt{3}} & 0 \\ 0 & 0 & 0 & 1 \end{bmatrix} \tag{30}$$

which satisfies $\mathbf{Q}^{-1} = \mathbf{Q}^{\mathrm{T}}$. The diagonal matrices $\mathbf{\Lambda}_D$ and $\mathbf{\Lambda}_P$ are given by

$$\mathbf{\Lambda}_D = \operatorname{diag}\left[\frac{E}{(1+\nu)}, \frac{E}{(1+\nu)}, \frac{E}{(1-2\nu)}, \frac{E}{2(1+\nu)}\right] \tag{31}$$

and

$$\mathbf{\Lambda}_P = \operatorname{diag}[0, 1, 0, 2] \tag{32}$$

respectively. Because the elastic stiffness matrix and the projection matrix have the same eigenvectors, the matrices $\mathbf{A}_{ij}$ simplify to

$$\mathbf{A}_{11} = \mathbf{Q}\left[\mathbf{I} + \frac{\Delta\lambda^{(i+1)}}{2\Psi}\mathbf{\Lambda}_D\mathbf{\Lambda}_P\right]\mathbf{Q}^{\mathrm{T}}$$

$$\mathbf{A}_{12} = -\frac{\Delta\lambda^{(i+1)}}{2\Psi}\mathbf{Q}\mathbf{\Lambda}_D\mathbf{\Lambda}_P\mathbf{Q}^{\mathrm{T}}$$

$$\mathbf{A}_{21} = -\frac{\Delta\lambda^{(i+1)}}{2\Psi}(1-\gamma)E_{\mathrm{ks}}\mathbf{Q}\mathbf{\Lambda}_M\mathbf{\Lambda}_P\mathbf{Q}^{\mathrm{T}}$$

$$\mathbf{A}_{22} = \mathbf{Q}\left[\mathbf{I} + \frac{\Delta\lambda^{(i+1)}}{2\Psi}(1-\gamma)E_{\mathrm{ks}}\mathbf{\Lambda}_M\mathbf{\Lambda}_P\right]\mathbf{Q}^{\mathrm{T}}$$

Setting

$$\mathbf{\Lambda}_{11} = \mathbf{I} + \frac{\Delta\lambda^{(i+1)}}{2\Psi}\mathbf{\Lambda}_D\mathbf{\Lambda}_P$$

$$\mathbf{\Lambda}_{12} = -\frac{\Delta\lambda^{(i+1)}}{2\Psi}\mathbf{\Lambda}_D\mathbf{\Lambda}_P$$

$$\mathbf{\Lambda}_{21} = -\frac{\Delta\lambda^{(i+1)}}{2\Psi}(1-\gamma)E_{\mathrm{ks}}\mathbf{\Lambda}_M\mathbf{\Lambda}_P$$

$$\mathbf{\Lambda}_{22} = \mathbf{I} + \frac{\Delta\lambda^{(i+1)}}{2\Psi}(1-\gamma)E_{\mathrm{ks}}\mathbf{\Lambda}_M\mathbf{\Lambda}_P$$

the mapping matrix can be written as

$$\begin{bmatrix} \mathbf{A}_{11} & \mathbf{A}_{12} \\ \mathbf{A}_{21} & \mathbf{A}_{22} \end{bmatrix} = \begin{bmatrix} \mathbf{Q} & \mathbf{0} \\ \mathbf{0} & \mathbf{Q} \end{bmatrix}\begin{bmatrix} \mathbf{\Lambda}_{11} & \mathbf{\Lambda}_{12} \\ \mathbf{\Lambda}_{21} & \mathbf{\Lambda}_{22} \end{bmatrix}\begin{bmatrix} \mathbf{Q}^{\mathrm{T}} & \mathbf{0} \\ \mathbf{0} & \mathbf{Q}^{\mathrm{T}} \end{bmatrix} \tag{33}$$

and the inverted mapping matrix is calculated as

$$\begin{bmatrix} \mathbf{A}_{11} & \mathbf{A}_{12} \\ \mathbf{A}_{21} & \mathbf{A}_{22} \end{bmatrix}^{-1} = \begin{bmatrix} \mathbf{Q} & \mathbf{0} \\ \mathbf{0} & \mathbf{Q} \end{bmatrix} \begin{bmatrix} \mathbf{\Lambda}_{11} & \mathbf{\Lambda}_{12} \\ \mathbf{\Lambda}_{21} & \mathbf{\Lambda}_{22} \end{bmatrix}^{-1} \begin{bmatrix} \mathbf{Q}^{\mathrm{T}} & \mathbf{0} \\ \mathbf{0} & \mathbf{Q}^{\mathrm{T}} \end{bmatrix} \tag{34}$$

with the inverted tridiagonal matrix given by

$$\begin{bmatrix} \mathbf{\Lambda}_{11} & \mathbf{\Lambda}_{12} \\ \mathbf{\Lambda}_{21} & \mathbf{\Lambda}_{22} \end{bmatrix}^{-1} = \begin{bmatrix} (\mathbf{\Lambda}_{11}\mathbf{\Lambda}_{22} - \mathbf{\Lambda}_{12}\mathbf{\Lambda}_{21})^{-1}\mathbf{\Lambda}_{22} & -(\mathbf{\Lambda}_{11}\mathbf{\Lambda}_{22} - \mathbf{\Lambda}_{12}\mathbf{\Lambda}_{21})^{-1}\mathbf{\Lambda}_{12} \\ -(\mathbf{\Lambda}_{11}\mathbf{\Lambda}_{22} - \mathbf{\Lambda}_{12}\mathbf{\Lambda}_{21})^{-1}\mathbf{\Lambda}_{21} & (\mathbf{\Lambda}_{11}\mathbf{\Lambda}_{22} - \mathbf{\Lambda}_{12}\mathbf{\Lambda}_{21})^{-1}\mathbf{\Lambda}_{11} \end{bmatrix} \tag{35}$$

The matrix product $(\mathbf{\Lambda}_{11}\mathbf{\Lambda}_{22} - \mathbf{\Lambda}_{12}\mathbf{\Lambda}_{21})^{-1}$ can be computed explicitly as

$$(\mathbf{\Lambda}_{11}\mathbf{\Lambda}_{22} - \mathbf{\Lambda}_{12}\mathbf{\Lambda}_{21})^{-1} = \left[\mathbf{I} + \frac{\Delta\lambda^{(i+1)}\mathbf{\Lambda}_D\mathbf{\Lambda}_P}{2\Psi} + \frac{\Delta\lambda^{(i+1)}(1-\gamma)E_{\mathrm{ks}}\mathbf{\Lambda}_M\mathbf{\Lambda}_P}{2\Psi}\right]^{-1} \tag{36}$$

With this procedure the return-mapping algorithm has been given and the updated stress vector and the updated back-stress vector are both expressed in terms of the inelastic multiplier and the trial state variables. This provides a scalar expression in the inelastic multiplier which has to be determined by enforcing the constraint condition

$$f(\boldsymbol{\sigma}^{(i+1)}, \boldsymbol{\eta}^{(i+1)}, \boldsymbol{\kappa}^{(i+1)}) = f(\Delta\lambda^{(i+1)}) = 0 \tag{37}$$

which can be solved with a local Newton–Raphson iteration. Since the gradient $J = \partial_{\Delta\lambda} f$ is expensive to calculate it is approximated by a secant Newton–Raphson method which needs only a few scalar evaluations to approximate the derivative by the secant stiffness. The initial gradient is calculated from the development of the yield function in a Taylor series, and reads

$$J^{(0)} = -\partial_{\sigma_{\mathrm{E}}} f^{\mathrm{T}}\, \mathbf{D}_{\mathrm{e}}\, \partial_{\sigma_{\mathrm{E}}} f - (1-\gamma)E_{\mathrm{k}} + \partial_{\kappa_{\mathrm{E}}} f \tag{38}$$

The set of non-linear equations following from the finite element discretization will be solved using the Newton–Raphson method. The non-linear problem is then linearized in a sequence of iterations until the problem is converged. The linearization of the equations results in the tangent stiffness matrix which plays an important role in the performance and robustness of the Newton–Raphson method. It has been emphasized by Simo and Taylor[20] that the quadratic convergence of Newton's method depends crucially on the consistent linearization of the stress resulting from the return-mapping algorithm to set up the tangent stiffness. The updated stress at the end of iteration $(i+1)$ reads

$$\boldsymbol{\sigma}^{(i+1)} = \mathbf{D}_{\mathrm{e}}\{\boldsymbol{\varepsilon}^{(i+1)} - {}^{t}\boldsymbol{\varepsilon}_{\mathrm{c}} - \Delta\lambda^{(i+1)}\partial_{\sigma} f\} \tag{39}$$

which is linearized by calculating the total derivative

$$\mathrm{d}\boldsymbol{\sigma}^{(i+1)} = \mathbf{D}_{\mathrm{e}}\{\mathrm{d}\boldsymbol{\varepsilon}^{(i+1)} - \mathrm{d}\lambda\, \partial_{\sigma} f - \Delta\lambda^{(i+1)}\, \partial^2_{\sigma\sigma} f\, \mathrm{d}\boldsymbol{\sigma}^{(i+1)}\} \tag{40}$$

With the consistency condition enforced at $(i+1)$

$$\mathrm{d}f = \partial_{\sigma} f^{\mathrm{T}}\mathrm{d}\boldsymbol{\sigma} + \partial_{\eta} f^{\mathrm{T}}\mathrm{d}\boldsymbol{\eta} + \partial_{\kappa} f\, \mathrm{d}\kappa = 0 \tag{41}$$

we obtain

$$\mathrm{d}\boldsymbol{\sigma}^{(i+1)} = \mathbf{H}\left\{\mathrm{d}\boldsymbol{\varepsilon}^{(i+1)} - \frac{1}{E_{\mathrm{s}}}\partial_{\sigma} f\, \partial_{\sigma} f^{\mathrm{T}}\, \mathrm{d}\boldsymbol{\sigma}^{(i+1)}\right\} \tag{42}$$

with the hardening parameter

$$E_{\mathrm{s}} = -\partial_{\kappa} f + (1-\gamma)E_{\mathrm{k}} \tag{43}$$

and the modified stiffness matrix

$$\mathbf{H} = [\mathbf{C}_e + \Delta\lambda^{(i+1)}\partial^2_{\sigma\sigma} f\,]^{-1} \tag{44}$$

The consistent tangent stiffness relation is finally computed using the Sherman–Morrison–Woodbury formula

$$\mathrm{d}\boldsymbol{\sigma}^{(i+1)} = \left[\mathbf{H} - \frac{\mathbf{H}\partial_\sigma f\,\partial_\sigma f^{\mathrm{T}}\mathbf{H}}{E_s + \partial_\sigma f^{\mathrm{T}}\mathbf{H}\partial_\sigma f}\right]\mathrm{d}\boldsymbol{\varepsilon}^{(i+1)} \tag{45}$$

## TOTAL FORMULATION

The fundamental difference between the total formulation of the constitutive model and the incremental formulation discussed in the previous paragraph is the formulation in strains rather than in strain rates. If an additive decomposition of the total strain vector is assumed into an elastic, reversible part $\boldsymbol{\varepsilon}_e$, and an inelastic, irreversible part $\boldsymbol{\varepsilon}_c$, the strain vector is given by

$$\boldsymbol{\varepsilon} = \boldsymbol{\varepsilon}_e + \boldsymbol{\varepsilon}_c \tag{46}$$

The stress vector in the final state is given by

$$\boldsymbol{\sigma} = \mathbf{D}_e\,\boldsymbol{\varepsilon}_e \tag{47}$$

with $\mathbf{D}_e$ the elastic stiffness matrix. The inelastic strain vector is dependent upon the assumption of the constitutive model and is in general a function of the strain vector.

The fundamental notion of the existence of a yield function is also used in the deformation theory of plasticity and the basic difference with the flow theory is the assumption that the plastic strain vector is given by a total formulation rather than by a rate formulation, i.e.

$$\boldsymbol{\varepsilon}_c = \lambda\,\partial_\sigma f \tag{48}$$

with the plastic multiplier $\lambda$ to be determined by satisfaction of the Kuhn–Tucker conditions

$$\lambda \geqslant 0, \quad f(\boldsymbol{\sigma}, \boldsymbol{\eta}, \mathbf{q}) \leqslant 0, \quad \lambda f(\boldsymbol{\sigma}, \boldsymbol{\eta}, \mathbf{q}) = 0 \tag{49}$$

The internal variables are again collected in a vector $\mathbf{q}$ and evolve according to the general hardening law

$$\mathbf{q} = \lambda\,\mathbf{h}(\boldsymbol{\sigma}, \boldsymbol{\eta}, \mathbf{q}) \tag{50}$$

The system of equations which is obtained after applying the Euler backward algorithm reads

$$\begin{aligned}
\boldsymbol{\varepsilon}^{(i+1)} &= {}^t\boldsymbol{\varepsilon} + \Delta\boldsymbol{\varepsilon}^{(i+1)} \\
\boldsymbol{\sigma}^{(i+1)} &= \mathbf{D}_e(\boldsymbol{\varepsilon}^{(i+1)} - \boldsymbol{\varepsilon}_c^{(i+1)}) \\
\boldsymbol{\varepsilon}_c^{(i+1)} &= \lambda^{(i+1)}\partial_\sigma f^{(i+1)} \\
\mathbf{q}^{(i+1)} &= \lambda^{(i+1)}\mathbf{h}^{(i+1)} \\
\boldsymbol{\eta}^{(i+1)} &= \lambda^{(i+1)}(1-\gamma)E_{\mathrm{ks}}\,\partial_\sigma g^{(i+1)}
\end{aligned} \tag{51}$$

with $E_{\mathrm{ks}}$ the secant stiffness modulus. The discrete Kuhn–Tucker conditions are given by

$$\begin{aligned}
\lambda^{(i+1)} &\geqslant 0 \\
f(\boldsymbol{\sigma}^{(i+1)}, \boldsymbol{\eta}^{(i+1)}, \mathbf{q}^{(i+1)}) &\leqslant 0 \\
\lambda^{(i+1)} f(\boldsymbol{\sigma}^{(i+1)}, \boldsymbol{\eta}^{(i+1)}, \mathbf{q}^{(i+1)}) &= 0
\end{aligned} \tag{52}$$

An elastic-predictor–plastic-corrector algorithm is again considered in which the elastic trial state is now assumed as

$$\begin{aligned} \boldsymbol{\varepsilon}_E &= {}^t\boldsymbol{\varepsilon} + \Delta\boldsymbol{\varepsilon}^{(i+1)} \\ \boldsymbol{\sigma}_E &= \mathbf{D}_e \boldsymbol{\varepsilon}_E \\ \boldsymbol{\eta}_E &= \mathbf{0} \\ \mathbf{q}_E &= \mathbf{0} \end{aligned} \tag{53}$$

Accordingly, the elastic trial strain vector $\boldsymbol{\varepsilon}_E$ now given by the total strain at time $(i+1)$ and in the elastic trial state the internal variables, collected in the vector $\mathbf{q}$, and the back-stress vector $\boldsymbol{\eta}$, are equal to zero. In this fashion the updated stress vector is computed in the same manner as in the algorithm for flow theory, but for a different definition of the trial state. Consequently, deformation-type plasticity models can be analysed without major modifications of the algorithm described for the flow theory of plasticity.

The damage in the material is reflected in the internal parameter $\kappa$ which can be derived from the assumption of work hardening

$$W_c = \boldsymbol{\xi}^T \boldsymbol{\varepsilon}_c = \bar{\sigma}(\gamma\kappa)\kappa$$

which can be elaborated as

$$\lambda = \kappa$$

The tangent stiffness matrix is again developed from the updated stress at $(i+1)$,

$$\boldsymbol{\sigma}^{(i+1)} = \mathbf{D}_e\{\boldsymbol{\varepsilon}^{(i+1)} - \lambda^{(i+1)}\partial_\sigma f\} \tag{54}$$

The total derivative then reads

$$\mathrm{d}\boldsymbol{\sigma}^{(i+1)} = \mathbf{D}_e\{\mathrm{d}\boldsymbol{\varepsilon}^{(i+1)} - \mathrm{d}\lambda\,\partial_\sigma f - \lambda^{(i+1)}\partial^2_{\sigma\sigma} f\,\mathrm{d}\boldsymbol{\sigma}^{(i+1)}\} \tag{55}$$

During the process of plastic loading the consistency condition has to be satisfied:

$$\mathrm{d}f = \partial_\sigma f^T\,\mathrm{d}\boldsymbol{\sigma} + \partial_\eta f^T\,\mathrm{d}\boldsymbol{\eta} + \partial_q f^T\,\mathrm{d}\mathbf{q} = 0$$

which can be elaborated to

$$\mathrm{d}\lambda = \frac{1}{E_s}\partial_\sigma f^T\,\mathrm{d}\boldsymbol{\sigma}^{(i+1)} \tag{56}$$

with the hardening parameter

$$E_s = -\partial_q f^T \mathbf{h} + (1-\gamma)E_k \tag{57}$$

The consistent tangent stiffness matrix is finally obtained by substituting equation (56) into equation (55) and reads

$$\mathrm{d}\boldsymbol{\sigma}^{(i+1)} = \left[\mathbf{H} - \frac{\mathbf{H}\partial_\sigma f\,\partial_\sigma f^T\mathbf{H}}{E_s + \partial_\sigma f^T\mathbf{H}\,\partial_\sigma f}\right]\mathrm{d}\boldsymbol{\varepsilon}^{(i+1)} \tag{58}$$

with the modified stiffness matrix

$$\mathbf{H} = [\mathbf{C}_e + \lambda^{(i+1)}\partial^2_{\sigma\sigma} f]^{-1} \tag{59}$$

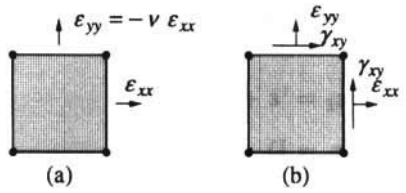


Figure 2. Tension–shear model problem: (a) tension up to cracking; (b) biaxial tension with shear beyond cracking

The limit of the consistent tangent stiffness matrix discussed for the model based on the flow theory of plasticity is also valid for deformation-type plasticity, because the structure of the yield function remains unaltered.

## TENSION–SHEAR MODEL PROBLEM

The fundamental differences of the formulations discussed in this study will be discussed with an elementary problem,[21] in which a plane-stress element with unit dimensions is loaded in biaxial tension and shear. This causes a continuous rotation of the principal strain axes after cracking, as is typical of crack propagation in smeared-crack finite element analysis. The element is subject to tensile straining in the $x$-direction accompanied by lateral Poisson contraction in the $y$-direction to simulate uniaxial loading. Immediately after the tensile strength has been violated, the element is loaded in combined biaxial tension and shear strain, see Figure 2. The ratio between the different strain components is given by $\Delta\varepsilon_{xx}:\Delta\varepsilon_{yy}:\Delta\gamma_{xy} = 0{\cdot}5:0{\cdot}75:1$. The Young's modulus of the concrete was taken as $E_c = 10\,000\ \mathrm{N/mm^2}$. Poisson's ratio was taken as $\nu = 0{\cdot}2$ and the tensile strength was assigned a unit value. A linear softening branch after the onset of cracking with a fracture energy $G_f = 0{\cdot}15 \times 10^{-3}\ \mathrm{N/mm}$ was adopted.

The behaviour of the different formulations for mode-I cracking which have been given in this study can be studied in detail with this problem. The constitutive behaviour will be compared with respect to the shear-stress–shear-strain behaviour and the normal-stress–normal-strain behaviour in the $x$- and $y$-directions. Particularly the shear-stress–shear-strain response gives a good impression of the behaviour of the model when applied to the analyses of plain or reinforced concrete structures. Standard fixed crack models show a continued hardening in this representation, while the multiple fixed crack model and the rotating crack model exhibit softening beyond some strain level.[8] The first issue which will be treated is the different behaviour of the models formulated in the total strain concept. The comparison between the rotating crack model and the deformation-type-based Rankine plasticity model with isotropic or kinematic hardening should elucidate whether the plasticity-based crack model is capable of predicting a flexible shear-stress–shear-strain response. The second issue is the comparison of the rotating crack model and the plasticity-based crack model within an incremental format. Because the response of models with a total formulation is in general more flexible than the response of models with an incremental formulation, it is expected that the Rankine plasticity model with an incremental formulation shows a less flexible shear-stress–shear-strain response, but the comparison should provide insight if this less flexible response is still acceptable.

The shear-stress–shear-strain response for different models described in a total format is shown in Figure 3. The standard fixed crack model has been used with a shear-retention factor equal to 0·05 which results in a monotonically increasing shear stress with increasing shear strain. The rotating crack model shows an implicit shear softening behaviour which has been observed

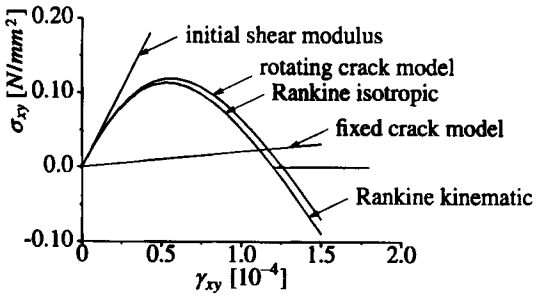


Figure 3. Total formulation of the constitutive models: $\sigma_{xy}$–$\gamma_{xy}$ response

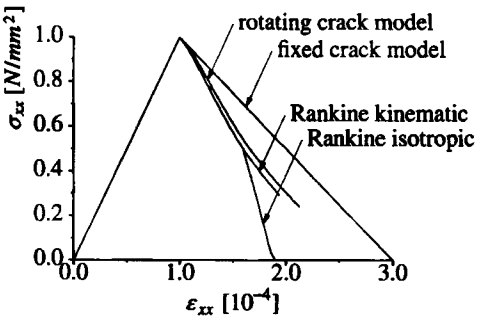


Figure 4. Total formulation of the constitutive models: $\sigma_{xx}$–$\varepsilon_{xx}$ response

previously by Rots[8] and by Willam *et al.*[21] It is interesting that the same behaviour occurs for the plasticity-based crack model with isotropic and kinematic hardening. The two formulations are in fact indiscernible until the shear stress has almost softened completely. Then, the isotropic and the kinematic hardening models yield different responses which is due to the fact that with isotropic softening it is impossible for the shear stress to become negative for positive increments of the shear strain component of the strain vector. It is obvious from Figure 3 that the differences between the deformation plasticity-based crack models and the rotating crack model are small. Only the fixed crack model gives a fundamentally different response.

The $\sigma_{xx}$–$\varepsilon_{xx}$ response depicted in Figure 4 shows that the input stress–strain softening diagram is exactly reproduced by the fixed crack model. This is logical, since the softening has been monitored in the fixed crack directions which are aligned with the $x, y$-axes. The behaviour of the other models shows an implicit normal-stress–shear-stress coupling. The Rankine plasticity model with isotropic hardening shows an increasing degradation of the stiffness when the stress has been decreased until approximately 50 per cent which is accompanied with a zero shear stress. At this stage the apex of the yield surface has been reached and the stress components in the $x$- and $y$-directions are softening in the direction of the origin. The response in the lateral $y$-direction is shown in Figure 5 which shows the formation of a secondary crack perpendicular to the first crack for the standard fixed crack model which again reflects the input softening diagram. The rotating crack model and the Rankine plasticity model with kinematic hardening show a gradual degradation of the stiffness in the $y$-direction. This can also be observed for the Rankine plasticity model with isotropic softening until the shear stress becomes equal to zero and the

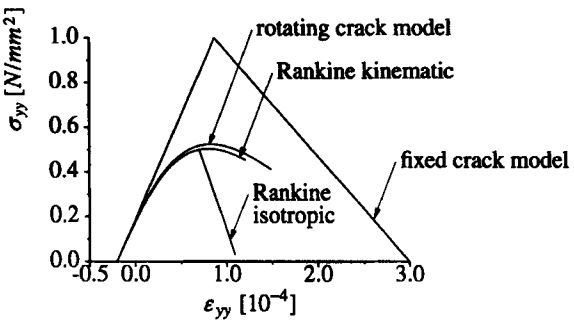


Figure 5. Total formulation of the constitutive models: $\sigma_{yy}$–$\varepsilon_{yy}$ response

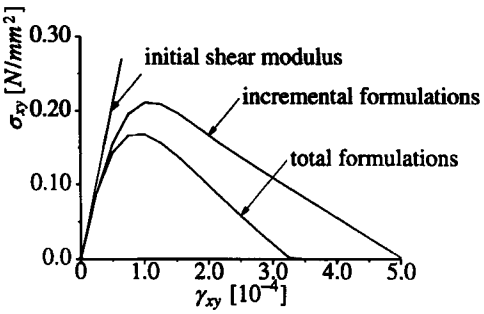


Figure 6. $G_f = \infty$: $\sigma_{xy}$–$\gamma_{xy}$ response

stress in the $y$-direction begins to soften linearly which is in accordance with the input softening diagram.

The limiting case with no softening ($G_f = \infty$) confirms that the different formulations within the total strain concept result in the same behaviour. The shear-stress–shear-strain responses of the rotating crack model and the Rankine plasticity model are shown in Figure 6. The response is identical for all models with a total formulation. It is clear from this figure that although no softening has been assumed, the shear-stress–shear-strain response shows an implicit softening behaviour. In Figure 6 the response of the Rankine model formulated within an incremental concept is also plotted. We observe a shear-stress–shear-strain response that is less flexible, but still shows an implicit shear softening.

The plasticity model based on an incremental formulation has also been applied to the tension–shear model problem with the *softening* material parameters and is compared with the rotating crack model in the following figures. The first interest concerns the behaviour in shear which is depicted in Figure 7. It is clear from Figure 7 that the rotating crack model has the most flexible response in shear, but the differences between the rotating crack model and the plasticity-based crack model are minor. Again, the Rankine plasticity model with isotropic hardening results in a shear stress equal to zero when the apex of the yield surface has been reached. The normal stress–strain response in the $x$-direction, see Figure 8, again shows an implicit normal-stress–shear-stress coupling for the models based on an incremental formulation. The normal-stress–normal-strain response in the lateral direction, Figure 9, shows a behaviour that is

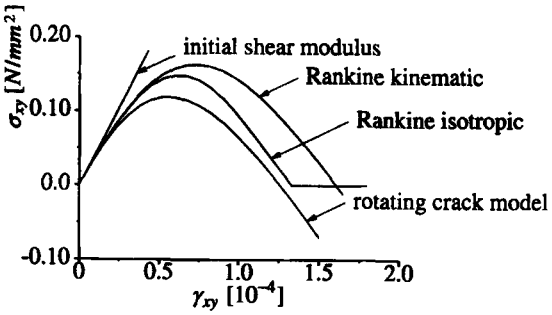


Figure 7. Incremental formulations and the rotating crack model: $\sigma_{xy}$–$\gamma_{xy}$ response

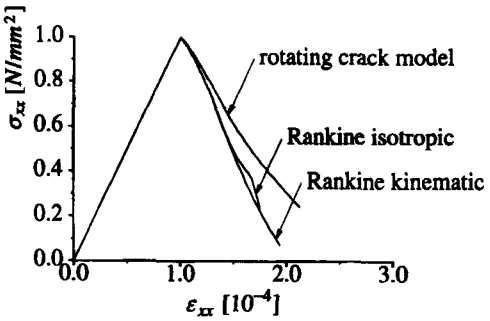


Figure 8. Incremental formulations and the rotating crack model: $\sigma_{xx}$–$\gamma_{xx}$ response

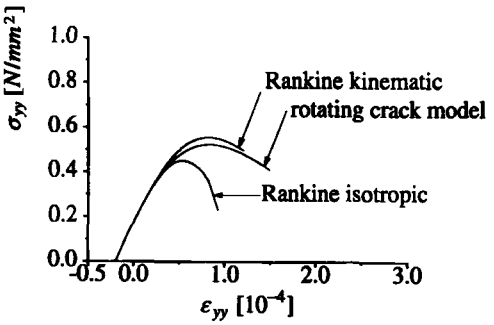


Figure 9. Incremental formulations and the rotating crack model: $\sigma_{yy}$–$\gamma_{yy}$ response

quite similar to that of the models based on the total formulation, cf. Figure 5. The response for the Rankine plasticity model with isotropic hardening again shows the linear softening relation when the apex of the yield surface has been reached. The response of the Rankine plasticity model with kinematic hardening shows a gradual degradation of the stiffness in the $y$-direction.

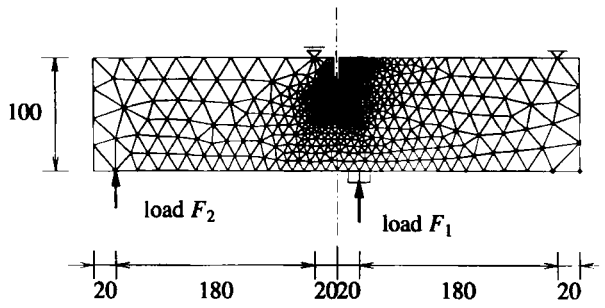


Figure 10. Finite element mesh for SEN beam; measures in mm

## APPLICATION TO PLAIN CONCRETE

The objective of the analyses presented here is to simulate curved mode-I fracture propagation with the rotating crack model and the plasticity-based crack models with isotropic and kinematic hardening/softening in an incremental format.

RILEM committee 89-FMT has proposed an experimental round robin using a Single Edge Notched (SEN) specimen to study the mixed-mode fracture process in plain concrete. The proposed experimental set-up has been improved such that the experiments could be performed without friction in the roller bearings.[22] The experiments show a curved crack propagating from the tip of the notch to the opposite side of the loading platen.

The scatter of the experimental results is small which makes the experiments very suitable for numerical simulation. The stress state in the specimen is mainly tension–shear with small compressive stresses, which justifies the assumption of linear elastic behaviour in compression, made implicitly in our crack model. However, it is noted that this assumption is not necessary, as the model has been augmented with a separate yield contour in the tension–compression and compression–compression regime.[23]

The SEN-specimen is $400 \times 100 \times 100$ mm$^3$ with a notch of $5 \times 20$ mm$^2$. The distance between the inner supports is equal to 40 mm and the distance between the outer supports is equal to 400 mm. The specimen has been discretized with 1655 three-noded plane-stress elements with a single integration point and a dense distribution of elements around the tip of the notch, Figure 10. The distribution of the loads has been modelled with $F_1 = \frac{10}{11}F$ at the centre loading platen and $F_2 = \frac{1}{11}F$ at the outer loading platen, with $F$ the total load. Only the centre loading platen has been modelled because only this platen has an influence on the stress distribution. The middle support has been fixed in the vertical direction and the outer support has been fixed in vertical and horizontal directions. The experiments on the small beams with normal weight concrete, maximum aggregate 8 mm, have been chosen for the numerical simulation. In accordance with the experimental data,[22] the following material parameters have been selected: $E_c = 35\,000$ N/mm$^2$, $\nu = 0{\cdot}15$, and tensile strength $f_{ct,m} = 2{\cdot}8$ N/mm$^2$. An exponential softening branch was used[23] with a fracture energy $G_f = 0{\cdot}07$ N/mm. The analyses have been performed using an advanced solution technique based on an incremental-iterative constrained Newton–Raphson method with line searches.[23] The convergence characteristics of the calculations were good, although for the rotating crack model a number of line searches appeared necessary.

The comparison of the experiment and the numerical simulations focuses on the Crack-Mouth-Sliding-Displacement (CMSD) versus the total load which should be considered as

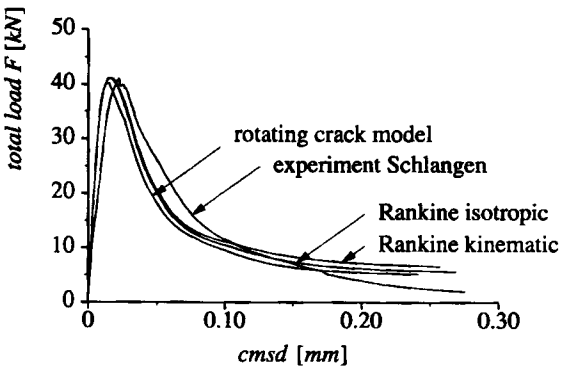


Figure 11. Load–CMSD diagram for SEN beam

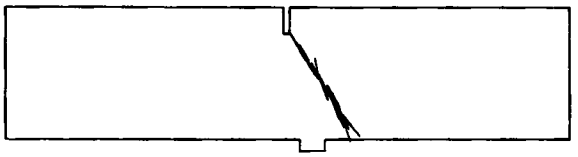

Figure 12. Crack pattern at final load for SEN beam

a representative measure of the non-linear behaviour of the structure. The total-load–CMSD diagram, Figure 11, shows a pre-peak behaviour which is a little too stiff for all models and a failure load which is in accordance with the experimental result. The post-peak behaviour is simulated within acceptable boundaries for all models. It appears that the different formulations of the constitutive models do not differ very much. At peak load the crack has initiated at the right-hand side of the notch with a direction of approximately 45° which has also been observed in the experiments.[21] At the final load the crack has propagated through the specimen from the notch to the right-hand side of the loading platen which is shown in Figure 12 for the analysis with the Rankine model with isotropic hardening. The crack pattern of the analysis with kinematic hardening or the rotating crack model is almost equal to the crack pattern of the Rankine model with isotropic hardening. The differences between the models are small and only perceptible in the final load stage.

## CONCLUSIONS

Two classes of plasticity-based crack models have been formulated, firstly within an incremental format and, secondly, with a total strain concept. In either case mixed hardening/softening was incorporated. As expected the deformation-type plasticity models show the most flexible response under loading paths where the principal strain axes rotate. Indeed, for the case of no hardening/softening the deformation theory coincides with the rotating crack model. Nevertheless, the fact that the crack model based on the flow theory of plasticity shows an only marginally less flexible response and the observation that it is easier to implement, make that the Rankine flow theory-based crack model is considered the best alternative. Moreover, it seems that the simpler case of pure isotropic hardening/softening can be used without significant loss of accuracy.

The Rankine-flow-theory-based crack model with isotropic hardening/softening not only performs well in simulations of mixed-mode crack propagation in plain concrete, as has been shown by a comparison with experiments, but it is also elegantly amenable for combination with other non-linear phenomena as creep, thermal effects, shrinkage, etc., it can be cast into a robust algorithm, and it can be combined rigorously with a plasticity model to bound the stresses in the tension–compression and the compression–compression regimes.

ACKNOWLEDGEMENTS

The calculations have been carried out with pilot versions of the DIANA finite element code. Financial support through the Commission of the European Communities under the Brite-EuRam programme (project BE-3275) and the Netherlands Technology Foundation (grant DCT72.1405) is gratefully acknowledged.

## APPENDIX I

*Stress update in the corner regime*

The stress update in the apex regime of the Rankine yield surface can be treated without modifications of the return-mapping procedure given in equation (24) with the explicitly computed inverted mapping matrix given in equation (34). The inverted mapping matrix is always determined even if the factor $\Psi$ is equal to zero. Without loss of generality it is shown here for isotropic hardening that the mapping procedure is unconditionally stable in the singular region of the yield surface. The matrix product $(\mathbf{A}_{11}\mathbf{A}_{22} - \mathbf{A}_{12}\mathbf{A}_{21})^{-1}$ now reduces to (cf. equation (36))

$$(\mathbf{A}_{11}\mathbf{A}_{22} - \mathbf{A}_{12}\mathbf{A}_{21})^{-1} = \left[\mathbf{I} + \frac{\Delta\lambda\,\mathbf{A}_D\mathbf{A}_P}{2\Psi}\right]^{-1} \tag{60}$$

and the inverted tridiagonal matrix becomes

$$\begin{bmatrix} \mathbf{A}_{11} & \mathbf{A}_{12} \\ \mathbf{A}_{21} & \mathbf{A}_{22} \end{bmatrix}^{-1} = \begin{bmatrix} 1 & 0 & 0 & 0 & 0 & 0 & 0 & 0 \\ 0 & \dfrac{\Psi}{\Psi + \Delta\lambda G} & 0 & 0 & 0 & \dfrac{\Delta\lambda G}{\Psi + \Delta\lambda G} & 0 & 0 \\ 0 & 0 & 1 & 0 & 0 & 0 & 0 & 0 \\ 0 & 0 & 0 & \dfrac{\Psi}{\Psi + \Delta\lambda G} & 0 & 0 & 0 & \dfrac{\Delta\lambda G}{\Psi + \Delta\lambda G} \\ 0 & 0 & 0 & 0 & 1 & 0 & 0 & 0 \\ 0 & 0 & 0 & 0 & 0 & 1 & 0 & 0 \\ 0 & 0 & 0 & 0 & 0 & 0 & 1 & 0 \\ 0 & 0 & 0 & 0 & 0 & 0 & 0 & 1 \end{bmatrix}$$

with $G = E/2(1 + \nu)$. Transformation from the eigenvector space to the stress space results in the limit

$$\lim_{\Psi \to 0} \begin{bmatrix} \mathbf{A}_{11} & \mathbf{A}_{12} \\ \mathbf{A}_{21} & \mathbf{A}_{22} \end{bmatrix}^{-1} = \begin{bmatrix} \frac{1}{2} & \frac{1}{2} & 0 & 0 & \frac{1}{2} & -\frac{1}{2} & 0 & 0 \\ \frac{1}{2} & \frac{1}{2} & 0 & 0 & -\frac{1}{2} & \frac{1}{2} & 0 & 0 \\ 0 & 0 & 1 & 0 & 0 & 0 & 0 & 0 \\ 0 & 0 & 0 & 0 & 0 & 0 & 0 & 1 \\ 0 & 0 & 0 & 0 & 1 & 0 & 0 & 0 \\ 0 & 0 & 0 & 0 & 0 & 1 & 0 & 0 \\ 0 & 0 & 0 & 0 & 0 & 0 & 1 & 0 \\ 0 & 0 & 0 & 0 & 0 & 0 & 0 & 1 \end{bmatrix} \tag{61}$$

so that the update of the stress vector is given by

$$\boldsymbol{\sigma}^{(i+1)} = \begin{bmatrix} \frac{1}{2} & \frac{1}{2} & 0 & 0 \\ \frac{1}{2} & \frac{1}{2} & 0 & 0 \\ 0 & 0 & 1 & 0 \\ 0 & 0 & 0 & 0 \end{bmatrix} \{\boldsymbol{\sigma}_{\mathrm{E}} - \tfrac{1}{2}\Delta\lambda \mathbf{D}_{\mathrm{e}} \boldsymbol{\pi}\} \tag{62}$$

see Figure 13. The return-mapping procedure is stable even in the corner regime where the stress is returned to the yield surface in approximately 10 iterations with an accuracy of $10^{-4}$ with respect to the initial equivalent stress. The calculation of the mapping matrix is also possible with a numerical scheme, e.g. Gauss decomposition, which results already in the limit of equation (62) even if the factor $\Delta\lambda/2\Psi$ is equal to 10. For this factor, with a Young's modulus equal to 30 000 N/mm$^2$ and a Poisson ratio equal to 0·15, the mapping matrix is given by

$$\left[\mathbf{I} + \frac{\Delta\lambda}{2\Psi}\mathbf{D}\mathbf{P}\right]^{-1} = \begin{bmatrix} 5{\cdot}000\mathrm{E}-01 & 5{\cdot}000\mathrm{E}-01 & 0{\cdot}000\mathrm{E}+00 & 0{\cdot}000\mathrm{E}+00 \\ 5{\cdot}000\mathrm{E}-01 & 5{\cdot}000\mathrm{E}-01 & 0{\cdot}000\mathrm{E}+00 & 0{\cdot}000\mathrm{E}+00 \\ 0{\cdot}000\mathrm{E}+00 & 0{\cdot}000\mathrm{E}+00 & 1{\cdot}000\mathrm{E}+00 & 0{\cdot}000\mathrm{E}+00 \\ 0{\cdot}000\mathrm{E}+00 & 0{\cdot}000\mathrm{E}+00 & 0{\cdot}000\mathrm{E}+00 & 3{\cdot}833\mathrm{E}-06 \end{bmatrix}$$

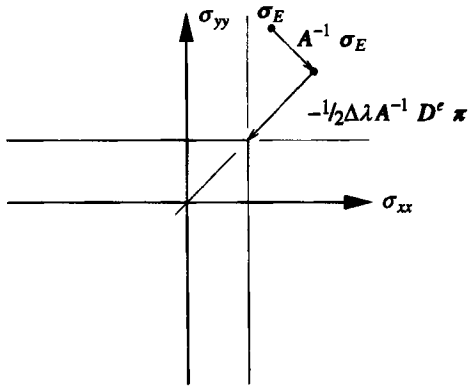


Figure 13. Return-mapping of the trial stress to the apex

which can be considered as accurate. The calculation of the inverted mapping matrix can now be performed with a numerical scheme in which the factor $\Delta\lambda/2\Psi$ should be less than or equal to 10.

The next issue which has to be treated for the apex is the modified stiffness matrix, equation (44), which is not defined in the apex of the yield surface. We first consider the second derivative of the yield function

$$\partial^2_{\sigma\sigma} f = \frac{\mathbf{P}}{2\Psi} - \frac{\mathbf{P}\boldsymbol{\xi}\boldsymbol{\xi}^{\mathrm{T}}\mathbf{P}}{4\Psi^3} \tag{63}$$

This expression becomes singular if $\Psi = (\frac{1}{2}\boldsymbol{\xi}^{\mathrm{T}}\mathbf{P}\boldsymbol{\xi})^{1/2}$ equals zero. Substitution of the second derivative in the expression for the modified stiffness matrix $\mathbf{H}$, equation (44), results after some algebraic manipulations in

$$\mathbf{H} = \left[\mathbf{C}_{\mathrm{e}} + \frac{\Delta\lambda}{2\Psi}\left(\mathbf{P} - \frac{1}{2\Psi^2}\mathbf{s}\mathbf{s}^{\mathrm{T}}\right)\right]^{-1} \tag{64}$$

with $\mathbf{s} = \mathbf{P}\boldsymbol{\xi}$. We now introduce the normalized vector $\hat{\mathbf{s}}$ such that

$$\mathbf{s} = \|\mathbf{P}\boldsymbol{\xi}\|\,\hat{\mathbf{s}} = (\boldsymbol{\xi}^{\mathrm{T}}\mathbf{P}\mathbf{P}\boldsymbol{\xi})^{1/2}\hat{\mathbf{s}} = (\beta\boldsymbol{\xi}^{\mathrm{T}}\mathbf{P}\boldsymbol{\xi})^{1/2}\hat{\mathbf{s}} = \Psi\sqrt{2\beta}\,\hat{\mathbf{s}} \tag{65}$$

with $\|\cdot\|$ designating the $L_2$-norm. For the Rankine criterion $\beta = 1 + 2\xi^2_{xy}/\mathbf{s}^{\mathrm{T}}\mathbf{s}$. With equation (65), the modified stiffness matrix becomes

$$\mathbf{H} = \left[\mathbf{C}_{\mathrm{e}} + \frac{\Delta\lambda}{2\Psi}(\mathbf{P} - \beta\hat{\mathbf{s}}\hat{\mathbf{s}}^{\mathrm{T}})\right]^{-1} \tag{66}$$

The apex of the yield surface is determined by the condition $\xi_{xx} = \xi_{yy}$; $\xi_{xy} = 0$. Then, the stress vector $\hat{\mathbf{s}}$ reduces to the null vector and the limit of the modified stiffness matrix in the apex is given by

$$\lim_{\Psi\to 0}\mathbf{H} = \lim_{\Psi\to 0}\left[\mathbf{C}_{\mathrm{e}} + \frac{\Delta\lambda}{2\Psi}\mathbf{P}\right]^{-1} = \mathbf{A}_{11}^{-1}\mathbf{D}_{\mathrm{e}} \tag{67}$$

because of the assumption of isotropic elasticity. The gradient of the yield surface is also not defined for the apex, but it is assumed that the gradient is given by

$$\partial_\sigma f = \tfrac{1}{2}\sqrt{2}\,\boldsymbol{\pi} \tag{68}$$

with the factor $\frac{1}{2}\sqrt{2}$ to obtain a consistent length of the gradient vector in the apex. Whereas the return-mapping algorithm is unconditionally stable even if the apex is encountered, the modified stiffness matrix cannot be calculated without a numerical approximation of the apex regime. It is therefore assumed in the algorithm for the calculation of the tangent stiffness matrix that a stress point lies within the apex region of the yield surface if the factor $\Psi$ becomes less than $10^{-4}$ times the initial equivalent stress.

## REFERENCES

1. Y. R. Rashid, 'Analysis of prestressed concrete pressure vessels', *Nucl. Eng. Design*, **7**, 334–344 (1968).
2. D. Ngo and A. C. Scordelis, 'Finite element analysis of reinforced concrete beams', *J. Am. Concrete Institute*, **64**, 152–163 (1967).
3. M. Suidan and W. C. Schnobrich, 'Finite element analysis of reinforced concrete', *J. Struct. Div. ASCE*, **99**, 2109–2122 (1973).

4. R. J. Cope, P. V. Rao, L. A. Clarke and P. Norris, 'Modelling of reinforced concrete behaviour for finite element analysis of bridge slabs', in C. Taylor, E. Hinton and D. R. J. Taylor (eds.), *Numerical Methods for Non-Linear Problems*, Pineridge Press, Swansea, 1980, pp. 457–470.
5. R. de Borst and P. Nauta, 'Non-orthogonal cracks in a smeared finite element model', *Eng. Comput.*, **2**, 35–46 (1985).
6. R. de Borst, 'Non-linear analysis of frictional materials', *Dissertation*, Delft University of Technology, 1986.
7. R. de Borst, 'Smeared cracking, plasticity, creep and thermal loading—a unified approach', *Comput. Methods Appl. Mech. Eng.*, **62**, 89–110 (1987).
8. J. G. Rots, 'Computational modeling of concrete fracture', *Dissertation*, Delft University of Technology, 1988.
9. M. A. Crisfield and J. Wills, 'Analysis of R/C panels using different concrete models', *J. Eng. Mech. Div. ASCE*, **115**, 578–597 (1989).
10. J. C. Simo, J. G. Kennedy and S. Govindjee, 'Non-smooth multisurface plasticity and viscoplasticity. Loading/unloading conditions and numerical algorithms', *Int. j. numer. methods eng.*, **26**, 2161–2185 (1988).
11. R. D. Krieg and D. B. Krieg, 'Accuracies of numerical solution methods for the elastic–perfectly plastic model', *J. Pressure Vessel Technol. ASME*, **99**, 510–515 (1977).
12. H. L. Schreyer, R. F. Kulak and J. M. Kramer, 'Accurate numerical solutions for elastic–plastic models', *J. Pressure Vessel Technol. ASME*, **101**, 226–234 (1979).
13. J. C. Simo and R. L. Taylor, 'A return mapping algorithm for plane stress elastoplasticity', *Int. j. numer. methods eng.*, **22**, 649–670 (1986).
14. M. Ortiz and E. P. Popov, 'Accuracy and stability of integration algorithms for elastoplastic constitutive relations', *Int. j. numer. methods. eng.*, **21**, 1561–1576 (1985).
15. R. de Borst and P. H. Feenstra, 'Studies in anisotropic plasticity with reference to the Hill criterion', *Int. j. numer. methods eng.*, **29**, 315–336 (1990).
16. J. C. J. Schellekens and R. de Borst, 'The use of the Hoffman yield criterion in finite element analysis of anisotropic composites', *Comput. Struct.*, **37**, 1087–1096 (1991).
17. R. de Borst, 'The zero-normal-stress condition in plane-stress and shell elastoplasticity', *Commun. appl. numer. methods*, **7**, 29–33 (1991).
18. R. de Borst, 'A generalisation of $J_2$-flow theory for polar continua', *Comput. Methods Appl. Mech. Eng.*, **103**, 347–362 (1993).
19. H. G. Matthies, 'A decomposition method for the integration of the elastic–plastic rate problem', *Int. j. numer. methods eng.*, **28**, 1–11 (1989).
20. J. C. Simo and R. L. Taylor, 'Consistent tangent operators for rate-independent elasto-plasticity', *Comput. Methods Appl. Mech. Eng.*, **48**, 101–118 (1985).
21. K. J. Willam, E. Pramono and S. Sture, 'Fundamental issues of smeared crack models', in S. P. Shah and S. E. Swartz (eds.), *Proc. SEM/RILEM Int. Conf. Fracture of Concrete and Rock*, Springer, New York, 1987, pp. 142–157.
22. E. Schlangen, Experimental and numerical analysis of fracture processes in concrete', *Dissertation*, Delft University of Technology, 1993.
23. P. H. Feenstra, 'Computational aspects of biaxial stress in plain and reinforced concrete', *Dissertation*, Delft University of Technology, 1993.